Microscopic and macroscopic manipulation of gold nanorod and its hybrid nanostructures [Invited]

Jiafang Li,* Honglian Guo, and Zhi-Yuan Li**

Laboratory of Optical Physics, Institute of Physics, Chinese Academy of Sciences, Beijing 100190, China
**Corresponding author: jiafangli@aphy.iphy.ac.cn*
***Corresponding author: lizy@aphy.iphy.ac.cn*

Received February 28, 2013; revised April 24, 2013; accepted April 24, 2013;
posted April 24, 2013 (Doc. ID 186163); published June 11, 2013

Gold nanorods (GNRs) have potential applications ranging from biomedical sciences and emerging nanophotonics. In this paper, we will review some of our recent studies on both microscopic and macroscopic manipulation of GNRs. Unique properties of GNR nanoparticles, such as efficient surface plasmon amplifications effects, are introduced. The stable trapping, transferring, positioning and patterning of GNRs with nonintrusive optical tweezers will be shown. Vector beams are further employed to improve the trapping performance. On the other hand, alignment of GNRs and their hybrid nanostructures will be described by using a film stretch method, which induces the anisotropic and enhanced absorptive nonlinearities from aligned GNRs. Realization and engineering of polarized emission from aligned hybrid GNRs will be further demonstrated, with relative excitation–emission efficiency significantly enhanced. Our works presented in this review show that optical tweezers possess great potential in microscopic manipulation of metal nanoparticles and macroscopic alignment of anisotropic nanoparticles could help the macroscopic samples to flexibly represent the plasmonic properties of single nanoparticles for fast, cheap, and high-yield applications.

OCIS codes: (350.4855) Optical tweezers or optical manipulation; (240.6680) Surface plasmons; (160.4236) Nanomaterials; (160.1190) Anisotropic optical materials.
http://dx.doi.org/10.1364/PRJ.1.000028

1. INTRODUCTION

Metal nanoparticles have a deep subwavelength size (usually less than 100 nm) that is much smaller than the wavelength of incident light. As they interact with incident light, electron density oscillations, so-called surface plasmons, will be localized around the nanoparticles. When the frequency of light matches the natural frequency of collective electron oscillations, localized surface plasmon resonance (SPR) will be excited [1,2]. The localized SPR modes strongly depend on three factors [3]: (a) the size, shape, composite, and topology of the particles; (b) the physical and chemical properties of the environment where the particles are embedded; and (c) the feature of the incident light, such as its polarization and propagation direction relative to the orientation of metal nanoparticles. When SPR occurs, the interaction of light with electron gas connected with plasmonic modes is significantly enhanced, leading to great enhancement of local electric field intensity and sensitivity of plasmonic mode response to environment. A direct consequence of local field enhancement, for example, is that when molecules located on metal nanoparticles are excited by incident light, their fluorescence and Raman signals can be significantly enhanced, with a fundamental goal to achieve single-molecule detection via these fingerprint signals [4]. There are many other benefits that originate from enhanced local field intensity at SPR. For instance, the classical scattering and absorption of light by metal nanoparticles can be greatly enhanced, leading to very large scattering and absorption cross sections [5]. Therefore, based on their unique localized SPR properties, metal nanoparticles have found potential applications ranging from biomedical sciences, catalysis, and sensing to information technology like imaging and data storage [2,6–10].

Since single metal nanoparticles are normally on a scale of sub-100-nm and difficult to be manipulated by conventional methods, studies on metal nanoparticles are normally involved with a lot of randomness in sample preparations [11]. The wide applications of metal nanoparticles are mainly based on their assemblies [9], in which the nanoparticles are randomly distributed. This causes an averaging issue in the case of anisotropic nanoparticles like gold nanorods (GNRs) [12], of which the anisotropy is always replaced by a macroscopically isotropic format. Meanwhile, recent studies have found that patterning of metal particles in certain forms could result in strong plasmonic couplings that generate novel plasmonic properties like Fano resonances [13–15], which is extremely sensitive in sensing applications. In these studies, people have fabricated metallic nanostructures, as the counterparts of metal nanoparticles, by employing traditional semiconductor nanofabrication techniques like electron beam lithography and focused ion beam lithography. However, these techniques are normally low-yield, expensive, and difficult to fabricate single-crystalline nanostructures [16]. In such a case, development of controllable methods to manipulate chemically synthesized metal nanoparticles is highly desirable.

In this review, we will briefly introduce our recent progress on the microscopic and macroscopic manipulation of GNRs with the optical tweezers and film stretch methods, respectively. In the next section, unique features of GNRs, such as efficient surface plasmon amplification effects, will be

briefly introduced. In the third section, the stable trapping, transferring, positioning, and patterning of gold nanoparticles with optical tweezers will be shown. Alignment of GNRs and their hybrid nanostructures in a macroscopic polymer film will be introduced in the fourth section and its applications on nonlinearity enhancement and polarized emission will also be demonstrated. Finally, this paper will be summarized in the fifth section.

2. UNIQUE PROPERTIES OF GOLD NANORODS

GNR is a cluster of gold atoms in a cylinder shape [12]. It has two axes, i.e., the transverse axis (along the short axis) and the longitudinal axis (along the long axis). The anisotropic shape of GNRs induces a splitting of the SPR into transverse and longitudinal SPR modes [17], compared with the single SPR mode of nanospheres, as shown in Figs. 1(a) and 1(b). Importantly, the longitudinal SPR of GNRs is extremely sensitive to the wavelength and polarization of the incident light. Compared with isotropic gold nanoparticles like gold nanoshells [18] and nanospheres, GNRs have small size and large optical cross sections at the longitudinal SPR wavelength, which is widely tunable in the visible to near-infrared wavelength range [Figs. 1(c) and 1(d)] [17,19]. Moreover, GNRs are very stable and can be synthesized in large quantities with various wet-chemical methods [12,19,20]. Therefore, GNRs have been demonstrated for potential applications ranging from biological imaging, sensing, and photothermal therapy to optical data storage, fluorescence enhancement, and plasmonic coupling devices, etc. [7,9–11,14,21,22].

The large optical cross sections but small volumes make GNRs a desirable candidate for the realization of surface plasmon amplification effects, i.e., "spaser" (surface plasmon amplification by stimulated emission of radiation) [23]. Since this concept was proposed by Bergman and Stockman in 2003 [24], many methods have been advanced to realize lasing spaser systems [25–28]. One effective method is to utilize the interaction between metallic nanoparticles and gain media. For example, gold nanospheres (GNSs) [28], gold nanocubes [29], and concentric spherical nanoparticles [25] incorporated with gain materials have been explored for the generation of spaser-like phenomena. However, the lasing wavelength of the spherical spaser-based nanolaser is limited by the narrowband SPR wavelength of the GNS. By utilizing the strong longitudinal SPR of GNRs, we have shown that GNRs are more efficient for building an active nanosystem for spasers with unique wavelength tunability and polarization sensitivity [23].

As illustrated in Fig. 2(a), the proposed active nanosystem based on GNRs is composed by GNR encapsulated by a silica shell doped with gain media. Such nanocomposites can be synthesized by an aqueous solution-based method [21]. In calculations, the core-shell particle was exposed in air with a refractive index $n_0 = 1.0$ and the refractive index of the shell was set as $n_{\text{shell}} = 1.5 - ik$. Here the "gain coefficient" k, which is related to the amplification coefficient of light intensity via $g = 4\pi k/\lambda$ [29], was introduced to describe the interaction strength between the incident light and the gain media. Under such a condition, the optical cross sections of extinction (C_{ext}), scattering (C_{scat}), and absorption (C_{abs}) for the GNR-based nanosystem were calculated with different gain coefficients using the discrete dipole approximation method

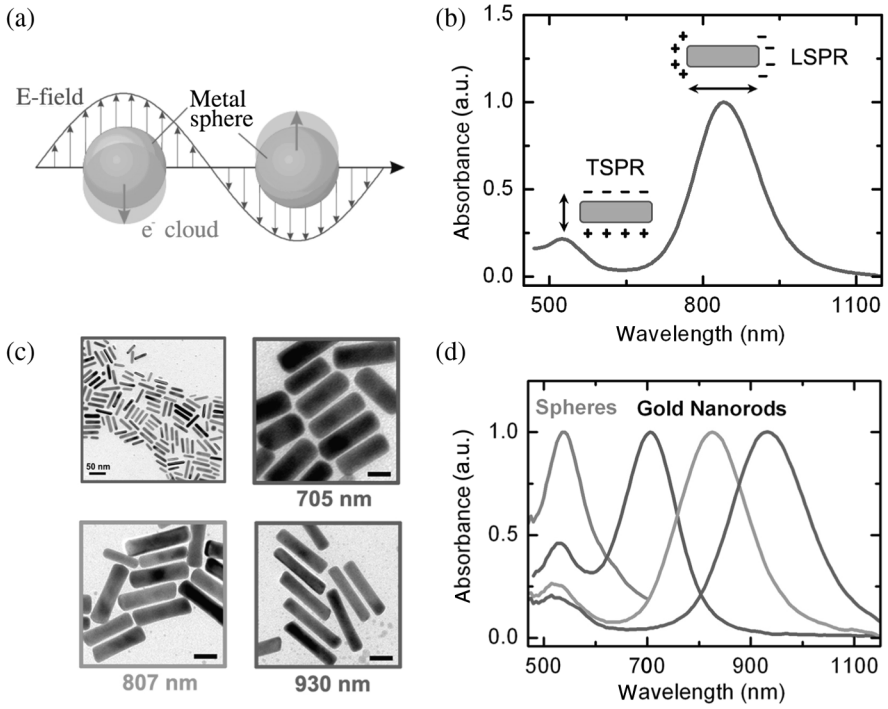

Fig. 1. (a) Schematic of plasmon oscillation for a nanosphere [1]. (b) Measured absorbance spectra of a GNR solution. The insets show the schematic of the transverse and longitudinal SPR modes, which correspond to two absorption peaks, respectively. (c) TEM images of as synthesized GNRs with different longitudinal SPR wavelength as noted [17]. (d) Measured absorbance spectra of gold nanospheres (GNSs) and GNRs, whose SEM images are shown in (c).

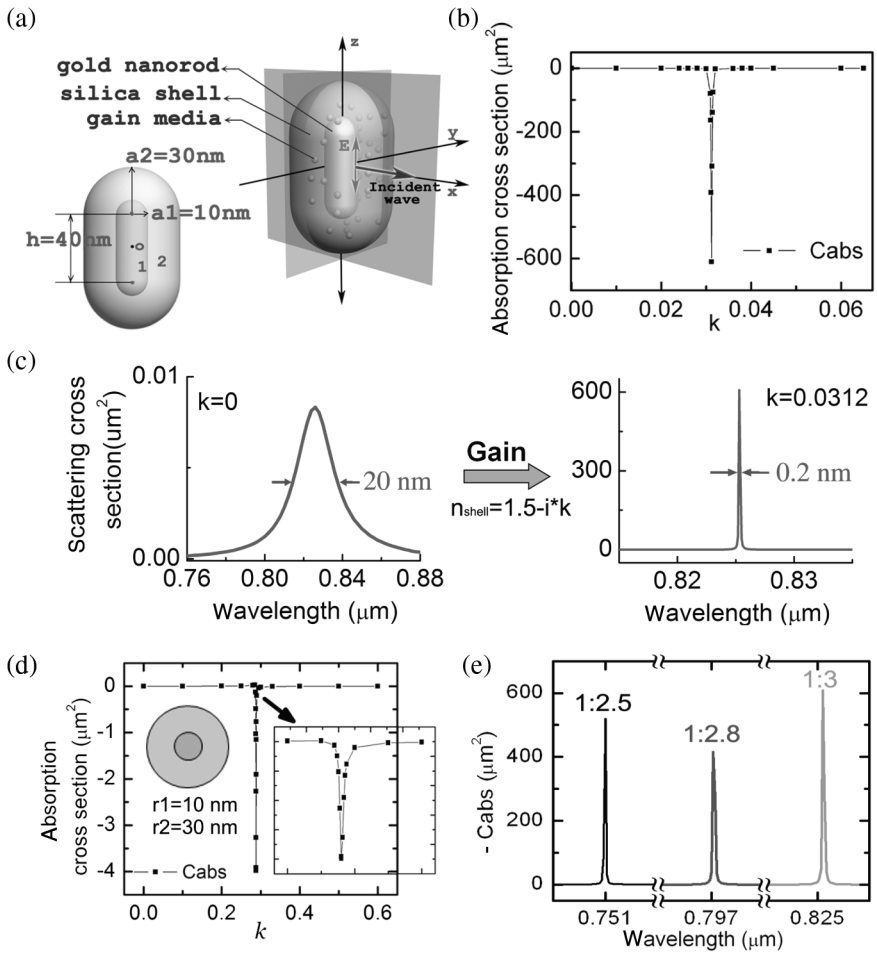

Fig. 2. (a) Schematic diagram of the GNR-based active nanosystem. (b) Calculated absorption cross section at the SPR wavelength of GNR as a function of gain coefficients (k). The spaser threshold is identified at $k = 0.0312$. (c) Calculated scattering cross section spectra for the nanosystem with different k as noted. At the spaser threshold, the scattering cross section is enhanced by $\sim 7 \times 10^4$ times and the linewidth is compressed by two orders of magnitude. (d) Calculated absorption cross section at the SPR wavelength of GNS-based nanosystem as a function of k. The spaser threshold is identified at $k = 0.288$. (e) Calculated wavelength-tunable spaser realized by varying the aspect ratio of the embedded GNR as noted [23].

[29]. It was found that C_{ext}, C_{scat}, and C_{abs} varied sensitively with k and there was a critical value of $k_c = 0.0312$, where C_{ext} at the SPR wavelength nearly reached the value of zero. At this critical point, as shown in Fig. 2(b), the absorption cross section becomes minus with extremely high absolute value ($\sim$600 μm^2), which indicates that a strong SPR amplification occurs. Under this condition, the peak value of C_{scat} reaches an extreme value of $\sim$600 μm^2, which is about 7×10^4 times the value when $k = 0$, as plotted in Fig. 2(c). Meanwhile, the SPR linewidth was significantly compressed by two orders of magnitude. The value of k_c can be called as the "threshold" for building up the strong amplification of SPR. While for the core-shell GNR the threshold was 0.0312, it was found that a similar GNS-based nanosystem has a threshold of 0.288 and at the threshold, the scattering cross section is only $\sim$3.8 μm^2, as shown in Fig. 2(d).

Figures 2(b) and 2(d) clearly indicate that the spaser threshold for the core-shell GNR is nearly one order of magnitude lower than that of the core-shell GNS. Meanwhile, at the spaser state, the absolute magnitude of the scattering cross section or absorption cross section of the GNR-based system ($\sim$600 μm^2) is more than 150 times larger than that of the GNS system ($\sim$3.8 μm^2). Therefore it can be inferred that taking GNR as the basic structure of the core-shell active nanosystem makes it much easier to realize spaser or great amplification of SPR. The low threshold of gain coefficient brings more choices of appropriate gain materials, such as dye molecules, rare earth ions, and semiconductor quantum dots. Moreover, it was found that by using the GNR-based nanosystem, the center wavelength of spasers can be widely tuned from the visible to near-infrared range via changing the aspect ratio of GNRs, as demonstrated in Fig. 2(e). In this way, a flexible wavelength-tunable spaser on nanoscale is possible.

So far, we have theoretically demonstrated the low-threshold generation of spaser by using GNR-based nanosystems. However, the direct experimental observation of the amplification effect of surface plasmon polaritons (SPPs) by the gain medium is still challenging and has aroused various ambiguities and controversies. The reason lies in the difficulties of direct recognition of the spontaneous emission (SE), amplified spontaneous emission (ASE), and lasing-like stimulated emission (LSE) of SPPs, as well as the direct photonic emission from the gain medium. To solve this puzzling problem, we have conducted experiments based on a typical

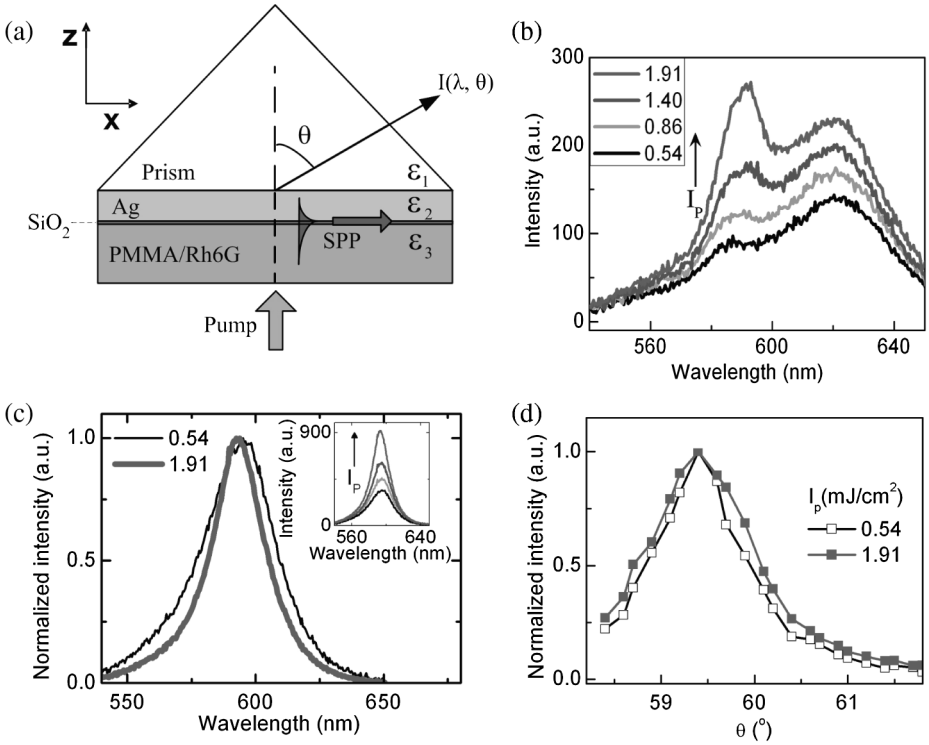

Fig. 3. (a) Schematic diagram of the experimental setup based on a typical Kretschmann system [30,31]. (b) Measured amplified emission spectra of SPPs decoupled at $\theta = 58.4°$. Spectra were measured with different I_P as noted (unit: mJ/cm^2). The ASE peak is clearly identified at $\lambda_{ASE} = 592.87$ nm [31]. (c) Normalized emission spectra of SPPs decoupled at $\theta = 59.2°$, where the spectra are peaked at the ASE wavelength ($\lambda_{ASE} = 592.87$ nm). Inset: measured emission spectra of SPPs under different I_P. With the increase of pump intensity, the ASE spectra are narrowed. (d) Angular distribution of SPP emission at wavelength 592.87 nm under different I_P as noted. It can be seen that with the increase of pump intensity, the angular response is broadened unusually [32].

Kretschmann configuration [Fig. 3(a)] [30,31]. The direct experimental evidence of ASE of SPPs (ASE_{SPP}) was observed at the interface of a silver film and a polymethyl methacrylate (PMMA) film doped with rhodamine 6G (Rh6G) dye molecules [Fig. 3(b)]. By carefully conducting a pump-dependent angle-resolved spectral measurement, the SE and ASE of SPPs, as well as the emission of Rh6G, have been successfully recognized [31]. The results provided a clear physical picture of the SPPs amplified by the gain medium. It turned out that the phenomenon reported in [30] may be actually an ASE instead of the LSE of SPPs. Moreover, it was found that, with the increase of pump intensity, the ASE spectra were narrowed as expected and predicted by many other reports, but the angular response ASE signals were broadened unusually [32], as shown in Figs. 3(c) and 3(d). These observations indicate that, although theoretical work can predicate the generation of spaser, there are still many nonclassical phenomena that need to be explored and understood. Further work is needed in this direction to figure out the ambiguities.

3. MICROSCOPIC MANIPULATION OF GOLD NANOPARTICLES WITH OPTICAL TWEEZERS

Optical tweezers, formed by a highly focused laser beam, have intriguing applications in biology and physics due to their unique characteristics of noncontact and nonintrusive manipulation of cells, subcells, micrometer-sized particles, and nanoparticles [32–39]. The trapping force is usually on the scale of piconewtons (10^{-12} N), which is very suitable for the study of dynamic properties of biological macromolecules, such as DNA [33], RNA [34], and proteins [35]. Moreover, in the field of physics it can be used for the study of Brownian motion of micrometer-sized beads, interactions between like-charge spheres, the motion of microspheres under a magnetic field, and positioning of GNSs [36–40]. By using a spatial light modulator (SLM), we have built up a system of SLM-based multi-optical traps and imaged the trapped particles in three dimensions clearly by several CCDs in large magnification, as shown in Fig. 4 [41]. In this system, the displacement of each particle can be precisely measured simultaneously and the trap stiffness can be measured by oscillating the sample stage in a triangle wave based on Stokes fluid dynamics [41]. The real-time manipulation and measurement of trapped objects built up a powerful platform for our studies on trapping of gold nanoparticles with optical tweezers.

A. Manipulation of GNRs by Optical Tweezers with Gaussian Beams

GNRs have attracted great interest due to their anisotropic SPRs, i.e., the longitudinal SPR and the transverse SPR. This anisotropy in SPR has afforded GNRs versatile advantages in both fundamental research and application potentials, such as the studies on plasmon couplings and five-dimensional information encodings [10,11]. It is also shown that the anisotropic GNRs can be stably trapped by a single optical trap [40]. However, for many applications, besides the trapping process, one needs to further transfer the GNR to desired targets or stabilize the GNRs on certain substrates [11,42], which has not been demonstrated.

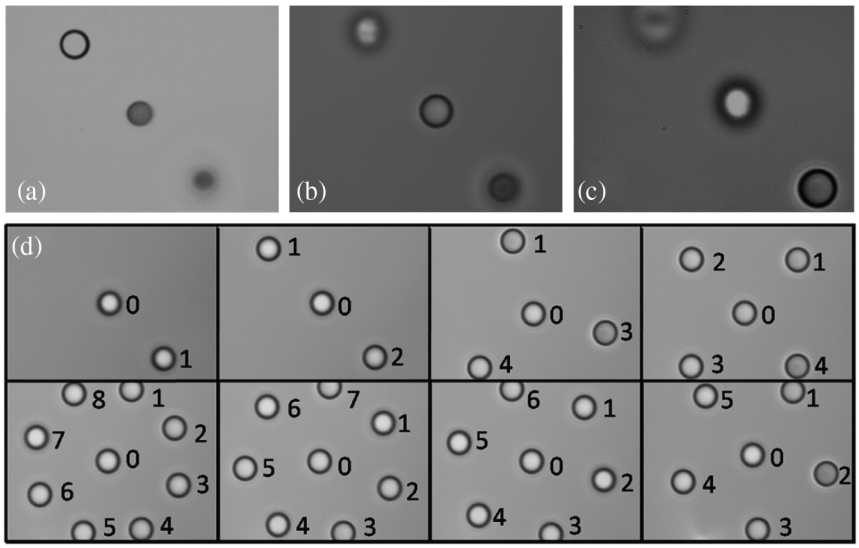

Fig. 4. (a)–(c) Pictures of three trapped polystyrene particles (2 μm in diameter) and their focused images in three dimensions. (d) Eight pictures of the trapped particles. The index number of each trap is indicated aside the trapped particle [41].

Recently we have successfully demonstrated the noninvasive manipulation of GNRs with a dual-optical trap [43]. By using the optical trapping forces formed by focused linearly polarized Gaussian beams, we show that GNRs can not only be freely trapped and transferred in water solution, but also be stably positioned and patterned on glass substrates. The studies could be helpful for applications of GNRs in the areas of *in vivo* biological studies, integrated plasmonic circuits, and complex plasmonic nanostructures in real nanoscale. For example, with the help of manipulation and positioning of GNRs, it is possible to pattern multiple GNRs with desired geometries that result in hybrid plasmonic resonances [11].

The setup used for trapping experiments is a home-built, dual-optical tweezers based on an inverted microscope [43], as illustrated in Fig. 5. Gold nanoparticles (bought from STREM) under manipulation by optical tweezers were dispersed in a sample chamber. The chamber was made by one ordinary coverslip (24 × 50 mm) and one polyvinyl alcohol (PVA) pretreated coverslip (22 × 22 mm). With the setup,

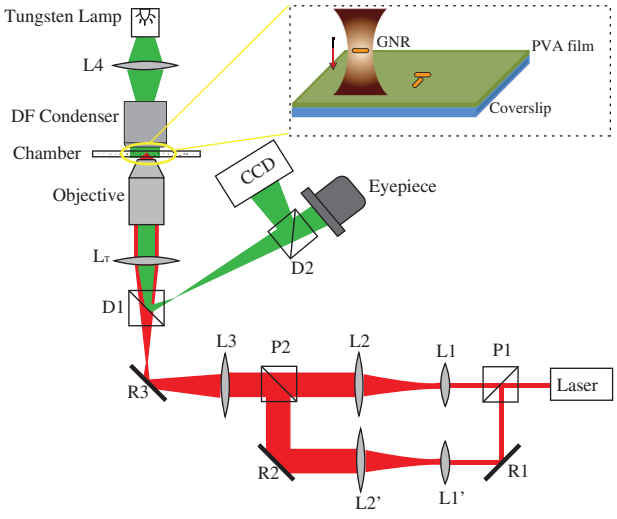

Fig. 5. Schematic diagram of the dual optical tweezers system [43].

gold nanoparticles were monitored by the dark field (DF) imaging system, in which the trapped particles could be monitored by eyepiece and CCD camera and the scattered light by the trapped particles can also be detected by using a spectrometer (Ocean Optics, QE 65000) to replace the CCD camera. As shown in Fig. 6, the DF images of trapped GNRs can be clearly recorded with the CCD camera. It should be mentioned that in this dual-optical tweezers system, one trap (Trap B) can be moved with a nanometer precision in the horizontal plane by rotating the reflecting mirror R2 driven by a DC servomotor (Newport, LTA-HL Actuator), while the other (Trap A) is fixed. As shown in Figs. 6(a)–6(c), GNRs can be stably trapped in Trap B and moved toward Trap A. By changing the trapping parameters, Trap B can even take over the originally trapped GNRs in Trap A, as illustrated in Fig. 6(d). Moreover, this trapping and transferring were reversible when Trap B was moved in back direction, as shown in Figs. 6(e)–6(h).

To position the trapped nanoparticles onto the desired substrate, a single GNR is trapped at a position about 10 μm above the bottom of the chamber, and then the trap moves down to contact the bottom surface and holds on for several seconds for the trapped GNR to be fixed on the bottom surface. Figure 7 shows the DF images of positioned and patterned gold nanoparticles by continuously transferring and fixing the trapped nanoparticles onto the substrate [43]. The Chinese character in Fig. 7(a) and "IOP" in Fig. 7(b) were "written" by GNRs. It should be mentioned that the patterned GNRs were very stable and kept unchanged even when one took out the solution from the chamber, dried the sample, performed other measurements, and repeated the trapping experiments. For example, in Fig. 7(b), the red "IOP" was "written" by using GNRs (25 × 73 nm in size) in the first positioning process and the green "CAS" was written by GNSs (50 nm in diameter) in the subsequent positioning process. It should be mentioned that the SPR peak positions for the GNS and GNRs were around 550 and 700 nm, respectively. That is why "CAS" made by nanospheres is green while "IOP" made by GNRs is red.

The sophisticated patterning GNRs on substrates with the optical traps provides a promising method for one to

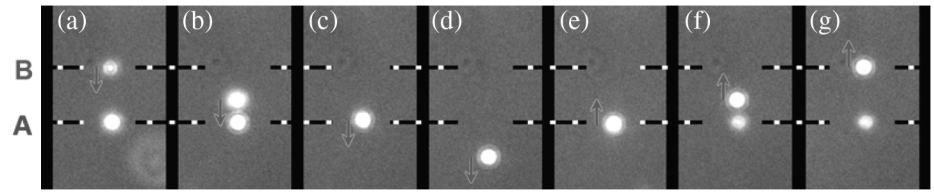

Fig. 6. DF images of trapping and transferring of GNRs with dual optical tweezers in water solution. The Trap B was moved top-down from (a) to (d) and bottom-up from (d) to (g).

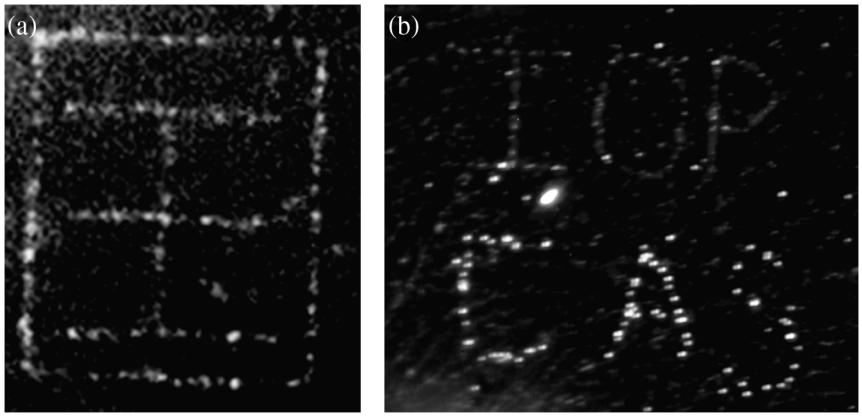

Fig. 7. Microscope images of positioning and patterning of gold nanoparticles. (a) Gray scaled picture of the patterned GNRs by optical trap on the bottom of the chamber. (b) Color picture of the patterned gold nanoparticles after the sample was dried [43]. The red "IOP" was "written" by GNRs first and the green "CAS" was "written" by GNSs subsequently on the same substrate.

pattern the GNRs more closely and form complex plasmonic structures that could lead to hybrid plasmon coupling effects [11,42]. Figure 8 shows the SEM images, measured DF scattering spectra, and calculated scattering spectra of positioned single and complex GNRs [43], respectively. It can be seen that when single GNRs [like in Fig. 8(a)] are manipulated to form complex structures [like the "T" shape in Fig. 8(d) and "end-to-end" configuration in Fig. 8(g)], their plasmonic properties are significantly different. The experimental and numerical results have clearly shown that complex patterns based on two GNRs as building blocks have already brought about many new plasmonic features that a single GNR cannot generate. These features originate from the coupling and hybridization of the two longitudinal dipolar modes excited in the two GNRs. By controlling the relative polarization state of laser light in the dual-optical tweezers, more controllable ways to generate complex shapes with small distances can be made based on two GNRs. In addition, since each GNR can have different diameters and lengths, a wide variety of geometric patterns with unique plasmonic properties can be readily generated by just using our dual-optical tweezers. In return, the technique can be further harnessed to produce versatile plasmonic nanostructures designed by computers based on desired SPR properties. In this regard, the dual-optical tweezers can become a versatile experimental "design" tool to create controllable patterns from colloidal GNRs rather than create the patterns accidentally by spin-coating a large number of GNRs randomly on a substrate [21].

B. Optical Trapping of Gold Nanoparticles by Cylindrical Vector Beams

Currently, most works on trapping and patterning gold nanoparticles use focused Gaussian beams. When a focused laser beam interacts with a small particle, a net momentum transfer from the laser to the particle produces optical force. The optical forces can be categorized into two types: one is scattering and absorption forces, which are proportional to the Poynting vector of the field and point along the direction of the incident beam, tending to destabilize the trap; the other is gradient force, which is proportional to the gradient of the light intensity and points toward the focus. For metallic particles, three dimensional trapping has been explored with different types of beams to reduce the negative influence caused by the scattering and absorption. For example, the optical forces on metallic particles produced by cylindrical vector beams have been calculated theoretically [44,45], and gold particles have been trapped experimentally by a radially polarized beam [46]. However, a quantitative comparison among optical trapping with different laser beams is still missing.

To experimentally realize stable optical trapping of gold nanoparticles by radially and azimuthally polarized beams, vector beams need to be generated first. To this aim, a polarization converter (ARCoptix, Switzerland) was inserted within the traditional optical tweezers system [47], which converted the linearly polarized Gaussian beam into a radially or azimuthally polarized beam, as shown in Fig. 9. With such a system, it was found that single 90 nm diameter GNS can be stably trapped in three dimensions successfully by both radially and azimuthally polarized beams. For comparisons, the transverse trapping stiffness of linearly, radially, and azimuthally polarized beams was measured, as shown in Fig. 10(a). The result shows that the radially polarized beam provides a larger transverse trapping stiffness than the Gaussian beam, while the stiffness for the azimuthally polarized beam is smaller [47]. Meanwhile, for both radially and azimuthally polarized

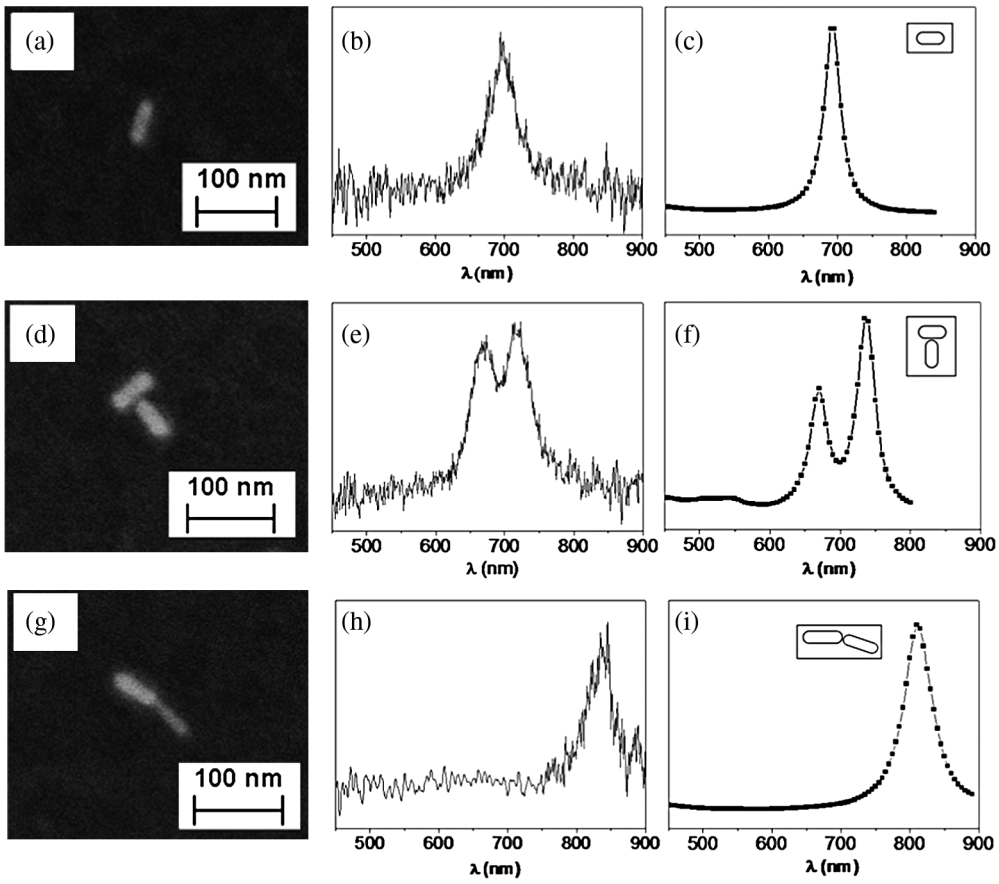

Fig. 8. SEM pictures of fixed single and complex GNRs and their scattering spectra [43]. (a) is the SEM picture of a fixed single GNR, (b) is the measured scattering spectrum of the fixed GNR after the sample was dried, (c) is the calculated scattering spectrum of a single GNR whose shape is shown in the upper right corner. (d)–(f) and (g)–(i) are the SEM pictures of two couples of the fixed GNRs, the measured scattering spectra and the calculated scattering spectra of the coupled GNRs.

beams, the transverse trapping stiffness increases linearly with the laser power [Fig. 10(b)]. The results can be understood as follows. For the radially polarized beam focused by a high numerical aperture objective, the electric field at the focus has an extremely strong axial component. This strong axial component is a nonpropagating field and does not contribute to the energy flow along the propagation direction. Therefore, a focused radially polarized beam provides a stronger gradient force to pull the gold particles toward the center of the focus while reducing the scattering and absorption force. That is why the stiffness is higher with the radially polarized beam. For the azimuthally polarized beam, the focus shape is a ring [48]. In such a case, the nanometer-sized gold particles might be trapped in the annular region of the focus. This successful trapping of gold nanoparticles by means of cylindrical vector beams and corresponding quantitative studies have opened up a new avenue to control and make use of the optical properties of metallic particles by means of optical tweezers [47].

4. ALIGNMENT OF GNRS IN MACROSCOPIC FILMS AND ITS APPLICATIONS

The studies on single metallic nanoparticles have aroused great interest due to their direct insight into various macroscopic plasmonic properties from a nanoscale point of view, such as plasmonic absorption, scattering, emission, and field localization. However, single nanoparticles are normally on a scale of sub-100-nm and are difficult to manipulate by conventional macroscopic methods. Therefore, wide applications of metallic nanoparticles are mainly based on their assemblies, in which the nanoparticles are randomly distributed. This causes an averaging issue in the case of anisotropic nanoparticles, of which the anisotropy is always replaced by a macroscopically isotropic format. For example, GNRs have attracted great attention due to their anisotropic SPR modes, i.e., the transverse (TSPR) and the longitudinal (LSPR) modes, which can be excited by light with polarization perpendicular and parallel to the rod, respectively. In most applications, only a portion of the GNRs with certain orientations was utilized because GNRs are naturally randomly oriented and their LSPR cannot be excited in the direction of incident light polarization perpendicular to their longitudinal axes. Moreover, the random distribution averages the microscopic anisotropy of the single GNR and the assembled GNRs behave like macroscopically isotropic materials. Therefore, macroscopically representing or constructively amplifying the anisotropic optical properties of a single GNR could be very preferable to improve the efficiency of GNR applications. Recently we found that by utilizing a well-developed film stretch method, both bare GNRs and hybrid GNRs nanostructures can be aligned in certain directions [17,49]. We show that this simple realization of alignment could directly bring out

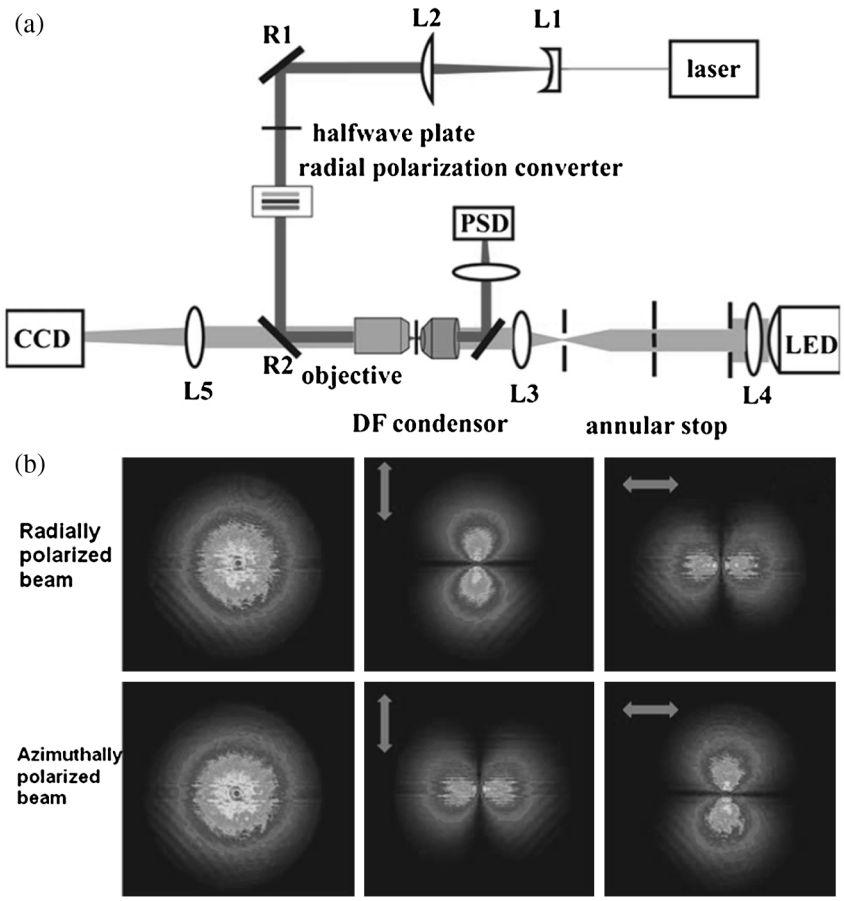

Fig. 9. (a) Schematic diagram of the optical trapping setup with cylindrical vector beams. The trapping laser was introduced into the polarized beam converter after expanding and focused to form a trap. (b) The experimentally generated radially and azimuthally polarized beams. The first column shows the isotropic intensity profiles of the vector beams imaged by a laser beam analyzer without a polarization analyzer. The next two columns show the intensity cross sections after inserting the polarization filter, with the arrows denoting the polarization direction [47].

two benefits: enhanced nonlinear absorption (NLA) for bare GNRs [17] and enhanced excitation–emission efficiency for hybrid GNRs with gain media [49].

A. Anisotropic and Enhanced Absorptive Nonlinearities from Aligned GNRs

The alignment of GNRs was realized by using a film stretch method [17,50]. For sample preparation, GNR water solution was synthesized by using a seed-mediated growth method [Fig. 1(c)] [19]. After the synthesis, the GNRs were purified and mixed with a 15% aqueous PVA solution by a volume ratio of 1:1. GNRs/PVA films were prepared by pouring the mixture into a Petri dish and then drying the samples naturally for 24 h at room temperature, which resulted in uniform polymer films with a thickness of ~100 μm [as illustrated in Fig. 11(a), the final thickness was dependent on the amount of the mixture

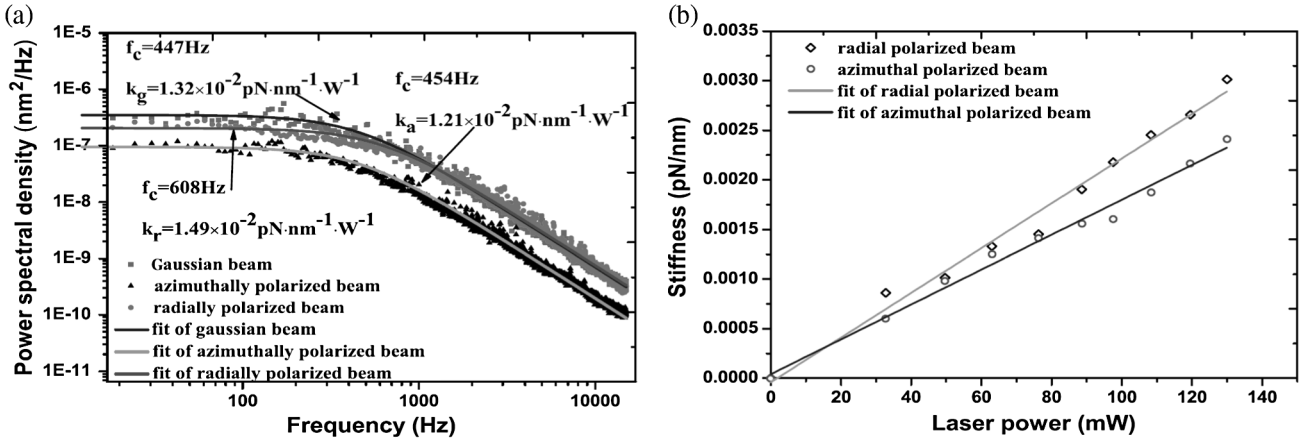

Fig. 10. (a) Power spectra of gold spheres with a diameter of 90 nm trapped by radially polarized, azimuthally polarized, and Gaussian beams measured by analyzing the Brownian motion of the particles. The stiffness in the figure is normalized by laser power. (b) Transverse trapping stiffness as a function of laser power for 90 nm gold particles trapped by radially and azimuthally polarized beams, respectively [47].

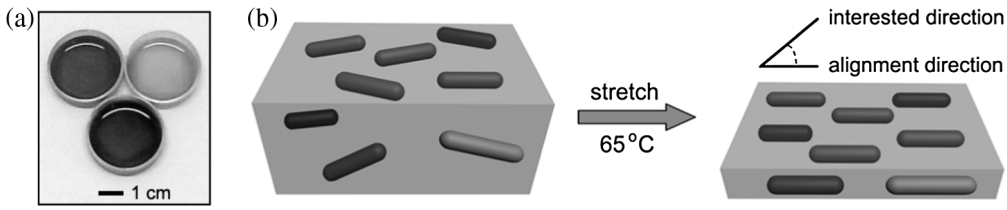

Fig. 11. (a) Camera picture of three GNRs/PVA films in Petri dish. (b) Schematic diagram of the film stretch process [17].

used]. Finally, the GNRs/PVA films were cut into a rectangular shape and manually stretched in one direction under heating at ~65°C [as schematically shown in Fig. 11(b)] until a desired length was obtained. In our experiments, the final length of the stretched film was chosen to be ~5 times its original length, which ensures the nearly complete alignment of GNRs inside the stretched films [50].

During the stretch process, the PVA molecules elongate along the stretch direction [51], which causes the longitudinal axes of GNRs orienting along the stretch direction. Because the LSPR mode is inherently polarized along the longitudinal axis, the stretched films will show collective LSPR when the incident light is polarized parallel to the stretch direction. As shown in Fig. 12(a), a stretched GNRs/PVA film shows distinct colors when the incident light is polarized parallel and perpendicular to the stretch direction, respectively, while the original film shows the same color in both polarization directions. These color displays are inherently associated with the corresponding absorption spectra, as plotted in Fig. 12(b). This splitting of the LSPR and TSPR in the macroscopic films could find useful applications in polarization-dependent color display devices [12].

For the nonlinear enhancement experiments, GNRs with large aspect ratios (~4) were used, of which the alignment was nearly perfect [Fig. 12(c)] and the LSPR and TSPR were well separated [Fig. 12(d)]. It should be mentioned that the measured SPR peaks and linewidth from macroscopic assembled GNRs matched well with the calculation of a single GNR, as shown in Figs. 12(d) and 12(e), which also indicates the narrow size distribution and the well alignment of GNRs.

The absorptive nonlinearities of various GNRs/PVA films were investigated by using the standard open-aperture Z-scan technique [52]. In the experiments, a pulsed laser (pulsewidth 3 ns) with a wavelength of 800 nm and a repetition rate of 10 Hz was used as the excitation source [17]. As shown in Fig. 13(a), the original GNRs/PVA film showed similar

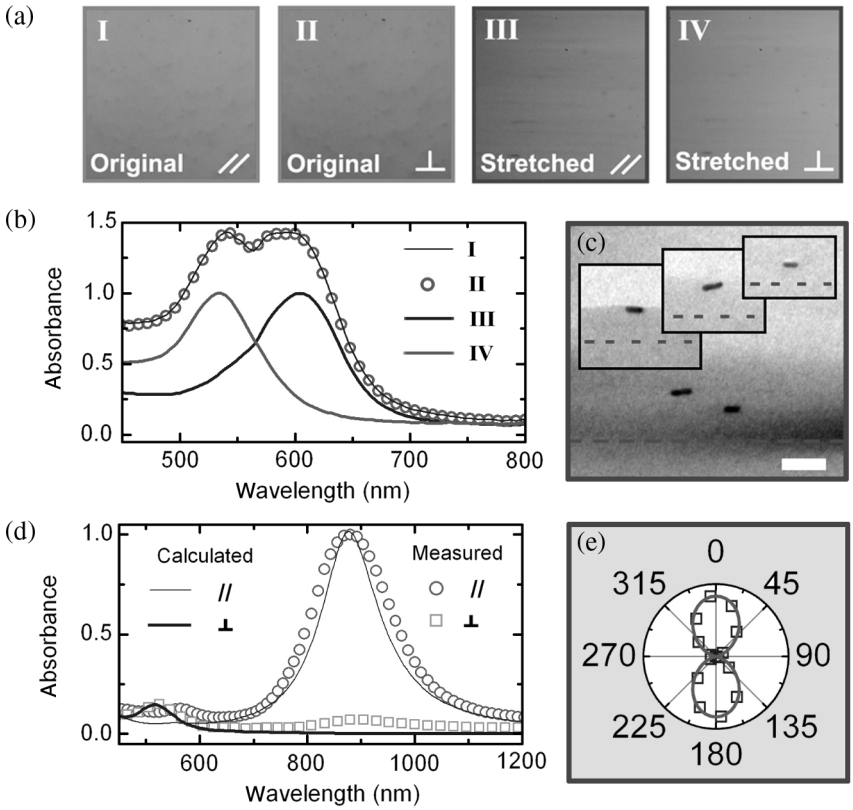

Fig. 12. (a) Optical microscope images of the original and stretched film under white light illumination with polarization parallel (‖) and perpendicular (⊥) to the stretch direction. (b) Measured absorbance spectra of the GNRs/PVA films corresponding to (a). (c) TEM images of the aligned GNRs in the PVA film. Scale bar: 100 nm. Dashed lines indicate the direction of stretch. (d) Measured absorbance spectra of another stretched GNRs/PVA film under excitation polarized parallel (‖) and perpendicular (⊥) to the stretch direction. Solid lines are the corresponding calculations of a single GNR. (e) Polar plot of the measured absorption intensity at wavelength 800 nm versus the excitation polarization angle. The solid curve is a fit to the cosine squared function [17].

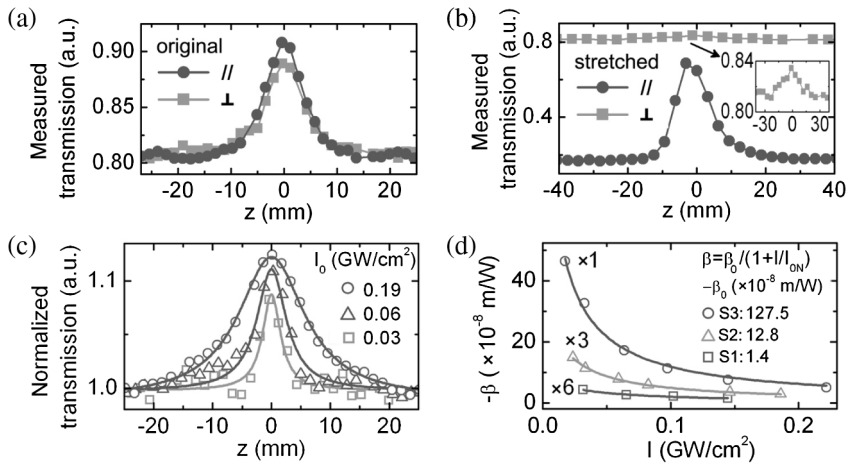

Fig. 13. (a), (b) Measured transmission of (a) original and (b) stretched GNRs/PVA films upon laser excitation polarized parallel (∥) and perpendicular (⊥) to the stretch direction, respectively. GNR concentrations (C_{GNR}) of the films: (a) 3.75 nmol/L and (b) 15 nmol/L. (c) Normalized transmission of a stretched GNRs/PVA film excited with different laser intensities. The laser polarization was along the stretch direction. Solid lines are corresponding fittings with the Z-scan theory. (d) NLA coefficient ($-\beta$) as a function of the laser intensity for three samples: (open square) S1: original film with $C_{GNR} = 3.75$ nmol/L; (open triangle) S2: stretched film with $C_{GNR} = 3.75$ nmol/L; (open circle) S3: stretched film with $C_{GNR} = 15$ nmol/L. The experimental data and their fittings (solid lines) were multiplied by corresponding numbers as noted for comparison purpose [17].

transmission responses upon the excitation with two different polarizations. While the linear absorption dominated in the region that was far away from the focus, the transmission peaks appearing at $z = 0$ were caused by the absorption saturation of the GNRs because of the high laser intensity near the focus. For a stretched film, on the other hand, there was a big difference in the Z-scan curves. In the case of parallel-polarized excitation, the NLA effects were very obvious while for the perpendicular-polarized excitation the NLA effects were very weak and difficult to characterize even after increasing the GNR concentration by four times [Fig. 13(b)].

To quantify the absorptive nonlinearity, the experimental data were normalized (to remove the effects of linear absorption) and fitted by using the Z-scan equation, with which the NLA coefficient β can be obtained [17]. β is defined by $\alpha(I) = \alpha + \beta I$, where $\alpha(I)$ is the intensity-dependent absorption coefficient including a linear absorption part α and a nonlinear part βI. For example, the fitted β values in Fig. 13(a) were $\beta_{\parallel} = -2.70 \times 10^{-8}$ m/W and $\beta_{\perp} = -2.59 \times 10^{-8}$ m/W, respectively. Therefore the macroscopic anisotropy factor of NLA can be evaluated by $\beta_{\parallel}/\beta_{\perp} = 1.04$, which indicates that this sample was nearly isotropic. Impressively, for the sample in Fig. 13(b), the anisotropic factor reached as high as ~20 ($\beta_{\parallel} = -7.23 \times 10^{-8}$ m/W, $\beta_{\perp} = -0.37 \times 10^{-8}$ m/W). Such strong anisotropy in nonlinearities can be attributed to the well-aligned GNRs in the stretched PVA films as well as the narrow size distribution of the colloidal GNRs.

Further experiments indicated that the Z-scan measurement was intensity dependent, as shown in Fig. 13(c). To ensure the accuracy in comparisons between different samples, we performed a series of intensity-dependent Z-scan measurements, deduced the corresponding β values, and fitted the obtained β data with a formula $\beta = \beta_0/(1 + I/I_{0N})$, where β_0 is the initial NLA coefficient under low-irradiance excitation and I_{0N} is the saturation irradiance of the NLA. As plotted in Fig. 13(d), the measured β values were well fitted with the formula, from which the values of β_0 were obtained for comparisons. For samples (S1 and S2) with the same GNR concentration it showed that the value of β_0 was enhanced by ~9 times by the simple stretch process. Moreover, it was noticed that the GNR concentration had a strong effect on the increase of β_0 value. After increasing the GNR concentration by 4 times, the β_0 value of the stretched film (sample S3) reached -127.5×10^{-8} m/W, which was about 91 times of that of the original film (S1).

The results indicated that the absorptive nonlinearities of the aligned GNRs were more than just the linear summation of the nonlinearities of individual GNR. This is reasonable because, besides the linearly summarized effects of separated GNRs, the plasmonic interaction between adjacent aligned GNRs is able to strengthen the local electric field and thus increase the NLA. Therefore, utilizing the plasmonic interactions and local field enhancement inside aligned GNR films provides an effective way to amplify the nonlinear effects of single GNRs. This work opened up a way to macroscopically represent and constructively amplify the optical properties of a single GNR, such as its anisotropy in nonlinearity enhancement. The enhanced absorptive nonlinearity could find promising applications in optical limiting, *Q*-switching, plasmonic waveguides, sensor protection, etc. [53–55].

B. Realization and Engineering of Polarized Emission from Aligned Hybrid GNRs

Polarized light emission is highly desirable in applications such as conventional light-emitting liquid crystal displays and emerging polarization-dependent nanophotonic devices [56–58]. Therefore, the realization of polarized light emission has been of great interest in the areas of photonics and material sciences. On one hand, polarized emission has been achieved by preparing emitting polymeric molecules aligned in certain direction [57,59,60]. On the other hand, the advanced development in nanotechnology has brought the realization of fluorescence polarization to a new regime. Functional photonic structures, such as photonic crystals [61] and metallic nanostructures [62], have been successfully utilized to directionally extract the emission signals from

various emitters to realize polarized emission. Since the operation bands of both nanoemitters (such as quantum dots and quantum rods) and nanostructures are widely tunable, these new methods are of great potential for the generation of broadband polarized emission. For example, in 2012 Rodriguez *et al.* realized polarized light emission from randomly distributed CdSe/CdS core/shell quantum rods by using silver nanoantenna arrays that were fabricated with substrate conformal imprint lithography [62]. However, lithographic methods are normally complicated, expensive, or low-yield. Therefore fast, simple, and high-yield realization of polarized emission with chemical methods is very desirable.

Recently we showed that macroscopic polarized light emission can be simply realized by aligning anisotropic hybrid GNR nanoparticles [49], which consist of GNRs in the core and dye molecule-doped silica in the shell. Compared with previous reports that used lithography and photobleaching methods, our samples can be prepared with a fast, simple, and high-yield chemical method. More importantly, by fully utilizing the LSPR of the hybrid GNRs, the relative excitation–emission efficiency of the macroscopic film can be enhanced by ~15 times. Moreover, the macroscopic film showed flexible polarization engineering capability. For instance, the film can convert circularly polarized light into broadband linearly polarized emission and tune the polarization contrast and directions of the linearly polarized emission [49]. The studies provide a simple but important method for the realization of polarized emission, as well as the easy application of active anisotropic nanoparticles.

The hybrid GNR nanoparticles (HGNRs) in our experiments were composed of GNRs in the core and dye molecules (Oxazine-725)-doped silica in the shell [as shown in the inset of Fig. 14(a), purchased from Nanoseedz], of which single nanoparticles have been studied for fluorescence enhancement and plasmon–molecule interactions [21,63,64]. For sample preparation, we used a film stretch method that we previously employed to align GNR metal particles [17], as illustrated in Fig. 11. To check the orientation of the HGNRs in the PVA films, the original and stretched films were sputtered with 15 nm gold and characterized with SEM. Before the alignment, nanoparticles were randomly distributed in the macroscopic films [Fig. 14(a)]. While after the film stretch process, the HGNRs were well aligned in the stretching direction, as shown in Figs. 14(b)–14(d). This is also reflected in Figs. 14(e) and 14(f), where the original film shows two extinction peaks irrespective of the light polarization directions while the stretched film possesses only one extinction peak upon each polarized excitation.

To study the emission properties of the macroscopic film, the sample was first excited with a circularly polarized pump at wavelength of 633 nm. It was found that when varying the angle of the detection polarization (α_{det}), the measured emission spectra show strong anisotropy. To avoid the cutoff effects of the long-pass filter, the emission intensity at the LSPR wavelength of 742 nm was monitored. As shown in Fig. 15(a), the emission intensity of the stretched sample varies periodically and can be well fitted using a cosine squared function together with an exponential decay that occurred when the detection polarization angle was continuously increased. This decay in intensity was due to the laser-induced photobleaching effects [21]. After calibrating the exponential decays, one can clearly see the dipole-like pattern in the polar plot of Fig. 15(b), which indicates an emission polarization close to linear polarization. By comparison, the emission from the original film shows only an exponential decay in Fig. 15(a), which is fully isotropic after calibration of the exponential decay [see Fig. 15(b)]. It should be mentioned that this polarized emission from the stretched film is not only observed at the wavelength of 742 nm but also seen at other wavelengths ranging from 650 to 880 nm. Therefore, the stretched macroscopic film could be useful for applications such as converting circularly polarized light into broadband linearly polarized emissions, as depicted in Fig. 15(c).

The aligned HGNRs are not only capable of realizing polarized emission but also helpful for obtaining the maximum excitation emission efficiency. As shown in Fig. 16(a), by exciting the sample with a linearly polarized pump (with polarization angle of θ_{ex}), the measured emission spectra were found to be highly dependent on the values of θ_{ex} and α_{det} as plotted in Fig. 16(b), where the symbols "∥" and "⊥" denote the angles of 0° and 90°, respectively. To compare the fluorescence efficiency among the different experimental

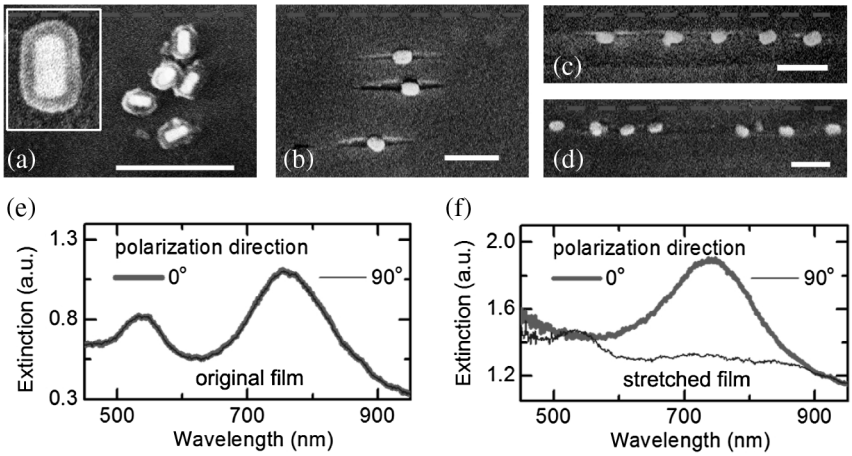

Fig. 14. (a)–(d) Typical SEM images of HGNRs in original (a) and stretched (b)–(d) PVA films. Inset: SEM image of a single core-shell GNR hybrid nanostructure (HGNR). The GNR in the core is ~95 nm in length and ~45 nm in diameter. After the stretch, most of the HGNRs in the film are aligned with long axis along the stretching direction (indicated by dash lines). Scale bars are 500 nm. (e) and (f) Measured extinction spectra of (e) original and (f) stretched film under incident light polarization parallel (0°) and perpendicular (90°) to the stretching direction [49].

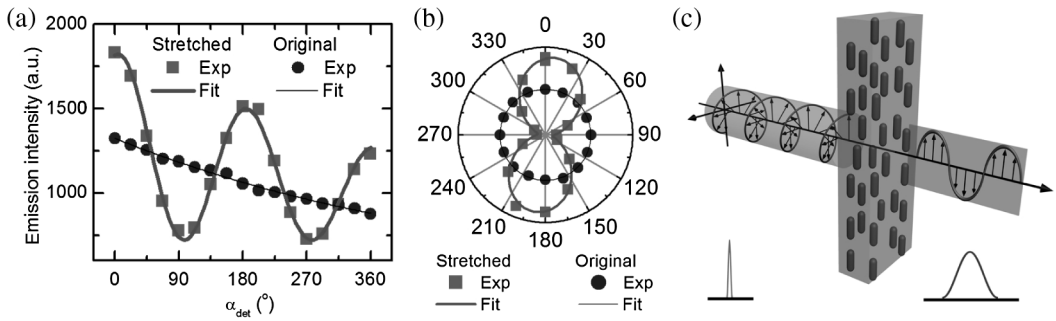

Fig. 15. (a) Measured emission intensity at wavelength 742 nm versus detection polarization angle (α_{det}) under excitation with circular polarization for the original and stretched film. The data are fitted with a cosine squared function together with an exponential decay. (b) Polar plot of the experimental and fitted data in (c) after calibrating the exponential decays. (c) Illustration of the applications of the stretched HGNRs for converting circularly polarized light into broadband linearly polarized emission [49].

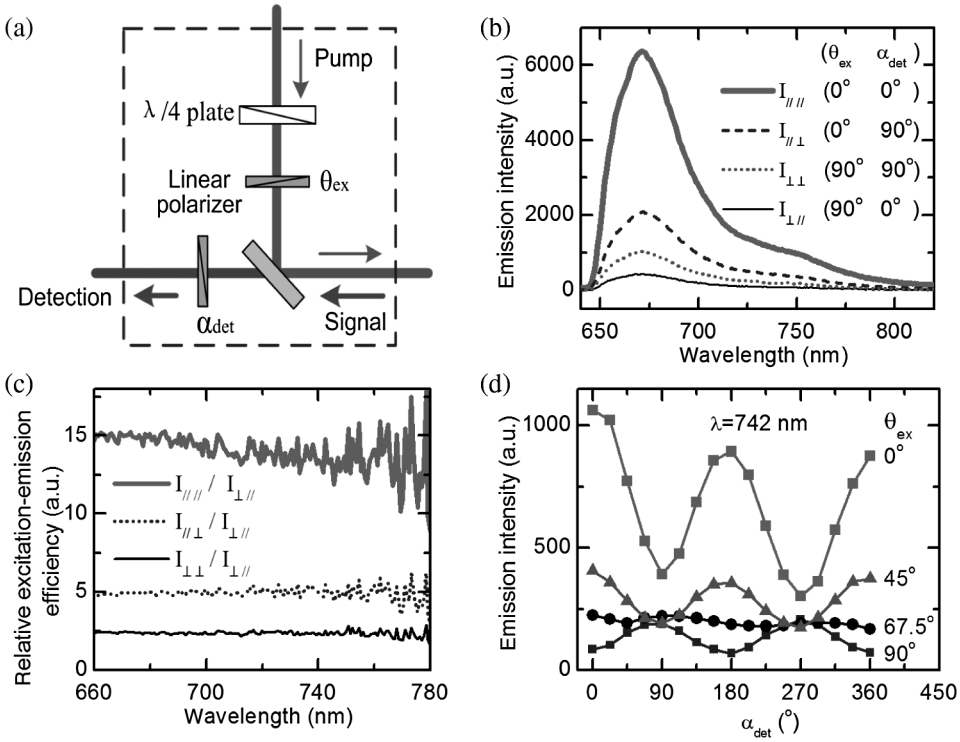

Fig. 16. (a) Schematic setup for emission measurements with different angles of detection polarization (α_{det}) under certain excitation polarization angles (θ_{ex}). (b) Measured emission spectra of the stretched film with different θ_{ex} and α_{det} as noted. The symbols "∥" and "⊥" denote the angles of 0° and 90°, respectively. The first and second subscripts represent the values of θ_{ex} and α_{det}, respectively. (c) Relative excitation emission efficiency of the emission spectra shown in (b). Spectra are normalized to the spectrum of $I_{\perp\parallel}$. (d) Measured emission intensity at 742 nm versus α_{det} under excitation with $\theta_{ex} = 0°$, 45°, 67.5°, and 90°, respectively [49].

schemes, the relative excitation emission efficiencies of the sample are calculated by normalizing the fluorescence spectra to the spectrum of $I_{\perp\parallel}$. As shown in Fig. 16(c), the highest relative efficiency (~15) is achieved when both the excitation and emission polarization directions are parallel to the stretching direction. Both Figs. 16(b) and 16(c) clearly demonstrate that, to obtain maximum polarized fluorescence from the stretched samples, the selection of both excitation and emission polarization is critical. The difference between the maximum ($I_{\parallel\parallel}$) and minimum ($I_{\perp\parallel}$) emission intensity can be as high as 15 times. The underlying physics is that because both the excitation and emission wavelengths are within the LSPR band of HGNRs [Fig. 14(f)], the excitation rate is increased due to the local field enhancement and the emission rate is enhanced by the increased local densities of optical states when the LSPRs are excited at both the excitation and emission wavelengths [63]. Therefore, both excitation and emission enhancement are induced and a maximum excitation emission efficiency is achieved.

It should be mentioned that not only the fluorescence efficiency but also the emission polarization can be controlled by using the aligned HGNRs [49]. Figure 16(d) plots the measured emission intensity at 742 nm versus α_{det} when exciting the stretched film with different angles of polarization. The polarization factors, simply defined as $PF = (I_{0°} - I_{90°})/(I_{0°} + I_{90°})$, are 0.5, 0.4, 0.01, and −0.4, respectively, for $\theta_{ex} = 0°$, 45°,

67.5°, and 90°. This indicates that when θ_{ex} increases from 0° to 45°, the polarization contrast of the emission is decreased, while at $\theta_{ex} = 67.5°$ the emission from the macroscopic film loses its polarization and behaves in an isotropic format (PF = 0.01). More interestingly, at $\theta_{ex} = 90°$, the PF changes to a minus value, which means that the polarization of the fluorescence is switched by 90°. This dependence of emission polarization on the excitation polarization is caused by the fact that not all GNRs were perfectly aligned during the film stretch method [17,50], as shown in Figs. 14(b)–14(d). As calculated from the data in Fig. 16(d) (after calibrating the background emission [49]), there are equivalently 10% HGNRs that are orientated in the perpendicular direction ($\theta_{ex} = 90°$) other than aligned. The LSPR of these not-aligned HGNRs can be excited by the perpendicular excitation and therefore shows different emission polarization from that of the aligned HGNRs. As a result, the emission polarization of the stretched film can be changed by varying the excitation polarization angles. These interesting observations offer the convenient feasibility to engineer the fluorescence polarization by controlling the excitation polarization.

5. CONCLUSIONS

In summary, we have introduced the microscopic manipulation of gold nanoparticles by using optical tweezers and the macroscopic application of GNRs by employing the film stretch method. On the one hand, our studies have clearly indicated that optical tweezers can become a noncontact and nonintrusive manipulation tool that is extremely promising for microscopic manipulation of metal nanoparticles. With the feasibility demonstrated in this review, further studies will focus on enhancing both the trapping stability and the positioning resolution, which are needed to overcome the negative effects caused by the Brownian motion and the strong absorption and scattering of the metal nanoparticles. In this case, the use of versatile vector beams, as already pointed out, could be a promising solution. On the other hand, our studies have convincingly shown that macroscopic alignment of group GNRs and HGNRs in polymer films can provide a fast, cheap, and high-yield approach for the applications of GNRs, such as macroscopic enhancement of absorptive nonlinearity and realization of polarized emission. This provides a novel idea that could help to macroscopically represent nanoscale plasmonic properties. More importantly, the idea is also applicable for a wide range of anisotropic nanoparticles (like nanorod, nanowires, nanobelts, etc.) made of metals (including gold, silver, copper, etc.) and their hybrid nanostructures incorporated with various active media like quantum dots, quantum rods, diamond particles, rare-earth ions, etc.

ACKNOWLEDGMENTS

This work is supported by the 973 Program of China (Nos. 2013CB632704 and 2013CB922404), the Knowledge Innovation Program of the Chinese Academy of Sciences (No. KJCX2-EW-W02), and the National Natural Science Foundation of China under Grant Nos. 11104342 and 61265010. The authors would like to thank Dr. Lin Gan, Dr. Lin Ling, Miss Si-Yun Liu, Lu Huang, Xiao-Lan Zhong, Ju Liu, Mr. Chen Wang, and Yu-Hui Chen for useful contributions.

REFERENCES

1. E. Hutter and J. H. Fendler, "Exploitation of localized surface plasmon resonance," Adv. Mater. **16**, 1685–1706 (2004).
2. K. A. Willets and R. P. Van Duyne, "Localized surface plasmon resonance spectroscopy and sensing," Annu. Rev. Phys. Chem. **58**, 267–297 (2007).
3. Z. Y. Li, "Nanophotonics in China: overviews and highlights," Front. Phys. **7**, 601–631 (2012).
4. S. Nie and S. R. Emory, "Probing single molecules and single nanoparticles by surface-enhanced Raman scattering," Science **275**, 1102–1106 (1997).
5. M. Hu, H. Petrova, A. R. Sekkinen, J. Chen, J. M. McLellan, Z.-Y. Li, M. Marquez, X. Li, Y. Xia, and G. V. Hartland, "Optical properties of Au–Ag nanoboxes studied by single nanoparticle spectroscopy," J. Phys. Chem. B **110**, 19923–19928 (2006).
6. M. Hu, J. Y. Chen, Z. Y. Li, L. Au, G. V. Hartland, X. D. Li, M. Marquez, and Y. N. Xia, "Gold nanostructures: engineering their plasmonic properties for biomedical applications," Chem. Soc. Rev. **35**, 1084–1094 (2006).
7. X. H. Huang, S. Neretina, and M. A. El-Sayed, "Gold nanorods: from synthesis and properties to biological and biomedical applications," Adv. Mater. **21**, 4880–4910 (2009).
8. M. T. Castaneda, S. Alegret, and A. Merkoci, "Electrochemical sensing of DNA using gold nanoparticles," Electroanalysis **19**, 743–753 (2007).
9. X. Li, T.-H. Lan, C.-H. Tien, and M. Gu, "Three-dimensional orientation-unlimited polarization encryption by a single optically configured vectorial beam," Nat. Commun. **3**, 998 (2012).
10. P. Zijlstra, J. W. M. Chon, and M. Gu, "Five-dimensional optical recording mediated by surface plasmons in gold nanorods," Nature **459**, 410–413 (2009).
11. A. M. Funston, C. Novo, T. J. Davis, and P. Mulvaney, "Plasmon coupling of gold nanorods at short distances and in different geometries," Nano Lett. **9**, 1651–1658 (2009).
12. J. Perez-Juste, I. Pastoriza-Santos, L. M. Liz-Marzan, and P. Mulvaney, "Gold nanorods: synthesis, characterization and applications," Coord. Chem. Rev. **249**, 1870–1901 (2005).
13. B. Luk'yanchuk, N. I. Zheludev, S. A. Maier, N. J. Halas, P. Nordlander, H. Giessen, and C. T. Chong, "The Fano resonance in plasmonic nanostructures and metamaterials," Nat. Mater. **9**, 707–715 (2010).
14. Z. K. Zhou, X. N. Peng, Z. J. Yang, Z. S. Zhang, M. Li, X. R. Su, Q. Zhang, X. Y. Shan, Q. Q. Wang, and Z. Y. Zhang, "Tuning gold nanorod-nanoparticle hybrids into plasmonic Fano resonance for dramaticallyenhanced light emission and transmission," Nano Lett. **11**, 49–55 (2011).
15. D. J. Wu, S. M. Jiang, Y. Cheng, and X. J. Liu, "Fano-like resonance in symmetry-broken gold nanotube dimer," Opt. Express **20**, 26559–26567 (2012).
16. J. S. Huang, V. Callegari, P. Geisler, C. Bruning, J. Kern, J. C. Prangsma, X. F. Wu, T. Feichtner, J. Ziegler, P. Weinmann, M. Kamp, A. Forchel, P. Biagioni, U. Sennhauser, and B. Hecht, "Atomically flat single-crystalline gold nanostructures for plasmonic nanocircuitry," Nat. Commun. **1**, 150 (2010).
17. J. Li, S. Liu, Y. Liu, F. Zhou, and Z. Y. Li, "Anisotropic and enhanced absorptive nonlinearities in a macroscopic film induced by aligned gold nanorods," Appl. Phys. Lett. **96**, 263103 (2010).
18. S. J. Oldenburg, R. D. Averitt, S. L. Westcott, and N. J. Halas, "Nanoengineering of optical resonances," Chem. Phys. Lett. **288**, 243–247 (1998).
19. B. Nikoobakht and M. A. El-Sayed, "Preparation and growth mechanism of gold nanorods (NRs) using seed-mediated growth method," Chem. Mater. **15**, 1957–1962 (2003).
20. F. Kim, J. H. Song, and P. D. Yang, "Photochemical synthesis of gold nanorods," J. Am. Chem. Soc. **124**, 14316–14317 (2002).
21. T. Ming, L. Zhao, Z. Yang, H. J. Chen, L. D. Sun, J. F. Wang, and C. H. Yan, "Strong polarization dependence of plasmon-enhanced fluorescence on single gold nanorods," Nano Lett. **9**, 3896–3903 (2009).
22. X. Li, F. J. Kao, C. C. Chuang, and S. L. He, "Enhancing fluorescence of quantum dots by silica-coated gold nanorods under one- and two-photon excitation," Opt. Express **18**, 11335–11346 (2010).

23. S. Y. Liu, J. F. Li, F. Zhou, L. Gan, and Z. Y. Li, "Efficient surface plasmon amplification from gain-assisted gold nanorods," Opt. Lett. **36**, 1296–1298 (2011).
24. D. J. Bergman and M. I. Stockman, "Surface plasmon amplification by stimulated emission of radiation: quantum generation of coherent surface plasmons in nanosystems," Phys. Rev. Lett. **90**, 027402 (2003).
25. J. A. Gordon and R. W. Ziolkowski, "The design and simulated performance of a coated nano-particle laser," Opt. Express **15**, 2622–2653 (2007).
26. X. F. Li and S. F. Yu, "Design of low-threshold compact Au-nanoparticle lasers," Opt. Lett. **35**, 2535–2537 (2010).
27. N. I. Zheludev, S. L. Prosvirnin, N. Papasimakis, and V. A. Fedotov, "Lasing spaser," Nat. Photonics **2**, 351–354 (2008).
28. M. A. Noginov, G. Zhu, A. M. Belgrave, R. Bakker, V. M. Shalaev, E. E. Narimanov, S. Stout, E. Herz, T. Suteewong, and U. Wiesner, "Demonstration of a spaser-based nanolaser," Nature **460**, 1110–1112 (2009).
29. Z. Y. Li and Y. N. Xia, "Metal nanoparticles with gain toward single-molecule detection by surface-enhanced Raman scattering," Nano Lett. **10**, 243–249 (2010).
30. M. A. Noginov, G. Zhu, M. Mayy, B. A. Ritzo, N. Noginova, and V. A. Podolskiy, "Stimulated emission of surface plasmon polaritons," Phys. Rev. Lett. **101**, 226806 (2008).
31. Y. H. Chen, J. F. Li, M. L. Ren, B. L. Wang, J. X. Fu, S. Y. Liu, and Z. Y. Li, "Direct observation of amplified spontaneous emission of surface plasmon polaritons at metal/dielectric interfaces," Appl. Phys. Lett. **98**, 261912 (2011).
32. Y. H. Chen, J. F. Li, M. L. Ren, and Z. Y. Li, "Amplified spontaneous emission of surface plasmon polaritons with unusual angle-dependent response," Small **8**, 1355–1359 (2012).
33. M. D. Wang, H. Yin, R. Landick, J. Gelles, and S. M. Block, "Stretching DNA with optical tweezers," Biophys. J. **72**, 1335–1346 (1997).
34. J.-D. Wen, M. Manosas, P. T. X. Li, S. B. Smith, C. Bustamante, F. Ritort, and I. Tinoco, Jr., "Force unfolding kinetics of RNA using optical tweezers. I. Effects of experimental variables on measured results," Biophys. J. **92**, 2996–3009 (2007).
35. P. Bechtluft, R. G. H. van Leeuwen, M. Tyreman, D. Tomkiewicz, N. Nouwen, H. L. Tepper, A. J. M. Driessen, and S. J. Tans, "Direct observation of chaperone-induced changes in a protein folding pathway," Science **318**, 1458–1461 (2007).
36. R. M. Simmons, J. T. Finer, S. Chu, and J. A. Spudich, "Quantitative measurements of force and displacement using an optical trap," Biophys. J. **70**, 1813–1822 (1996).
37. W. R. Bowen and A. O. Sharif, "Long-range electrostatic attraction between like-charge spheres in a charged pore," Nature **393**, 663–665 (1998).
38. W. Wen, L. Zhang, and P. Sheng, "Planar magnetic colloidal crystals," Phys. Rev. Lett. **85**, 5464–5467 (2000).
39. A. A. R. Neves, A. Camposeo, S. Pagliara, R. Saija, F. Borghese, P. Denti, M. A. Iatì, R. Cingolani, O. M. Maragò, and D. Pisignano, "Rotational dynamics of optically trapped nanofibers," Opt. Express **18**, 822–830 (2010).
40. L. Tong, V. D. Miljković, and M. Käll, "Alignment, rotation, and spinning of single plasmonic nanoparticles and nanowires using polarization dependent optical forces," Nano Lett. **10**, 268–273 (2010).
41. L. Ling, H. L. Guo, L. Huang, E. Qu, Z. L. Li, and Z. Y. Li, "The measurement of displacement and optical force in multi-optical tweezers," Chin. Phys. Lett. **29**, 014214 (2012).
42. R. A. Nome, M. J. Guffey, N. F. Scherer, and S. K. Gray, "Plasmonic interactions and optical forces between Au bipyramidal nanoparticle dimers," J. Phys. Chem. A **113**, 4408–4415 (2009).
43. L. Ling, H. L. Guo, X. L. Zhong, L. Huang, J. F. Li, L. Gan, and Z. Y. Li, "Manipulation of gold nanorods with dual-optical tweezers for surface plasmon resonance control," Nanotechnology **23**, 215302 (2012).
44. Q. Zhan, "Trapping metallic Rayleigh particles with radial polarization," Opt. Express **12**, 3377–3382 (2004).
45. J.-Q. Qin, X.-L. Wang, D. Jia, J. Chen, Y.-X. Fan, J. Ding, and H.-T. Wang, "FDTD approach to optical forces of tightly focused vector beams on metal particles," Opt. Express **17**, 8407–8416 (2009).
46. A. Huss, A. M. Chizhik, R. Jäger, A. I. Chizhik, and A. J. Meixner, "Optical trapping of gold nanoparticles using a radially polarized laser beam," Proc. SPIE **8097**, 809720 (2011).
47. L. Huang, H. Guo, J. Li, L. Ling, B. Feng, and Z.-Y. Li, "Optical trapping of gold nanoparticles by cylindrical vector beam," Opt. Lett. **37**, 1694–1696 (2012).
48. F. Peng, B. Yao, S. Yan, W. Zhao, and M. Lei, "Trapping of low-refractive-index particles with azimuthally polarized beam," J. Opt. Soc. Am. B **26**, 2242–2247 (2009).
49. S. Y. Liu, J. F. Li, and Z. Y. Li, "Macroscopic polarized emission from aligned hybrid gold nanorods embedded in a polyvinyl alcohol film," Adv. Opt. Mater. **1**, 227–231 (2013).
50. B. M. I. van der Zande, L. Pages, R. A. M. Hikmet, and A. van Blaaderen, "Optical properties of aligned rod-shaped gold particles dispersed in poly(vinyl alcohol) films," J. Phys. Chem. B **103**, 5761–5767 (1999).
51. D. Fornasiero and F. Grieser, "A linear dichroism study of colloidal silver in stretched polymer-films," Chem. Phys. Lett. **139**, 103–108 (1987).
52. M. Sheikbahae, A. A. Said, T. H. Wei, D. J. Hagan, and E. W. Vanstryland, "Sensitive measurement of optical nonlinearities using a single beam," IEEE J. Quantum Electron. **26**, 760–769 (1990).
53. R. West, Y. Wang, and T. Goodson, "Nonlinear absorption properties in novel gold nanostructured topologies," J. Phys. Chem. B **107**, 3419–3426 (2003).
54. L. Francois, M. Mostafavi, J. Belloni, and J. A. Delaire, "Optical limitation induced by gold clusters: mechanism and efficiency," Phys. Chem. Chem. Phys **3**, 4965–4971 (2001).
55. S. A. Maier, P. G. Kik, H. A. Atwater, S. Meltzer, E. Harel, B. E. Koel, and A. A. G. Requicha, "Local detection of electromagnetic energy transport below the diffraction limit in metal nanoparticle plasmon waveguides," Nat. Mater. **2**, 229–232 (2003).
56. K. Kogo, T. Goda, M. Funahashi, and J. Hanna, "Polarized light emission from a calamitic liquid crystalline semiconductor doped with dyes," Appl. Phys. Lett. **73**, 1595–1597 (1998).
57. K. S. Whitehead, M. Grell, D. D. C. Bradley, M. Inbasekaran, and E. P. Woo, "Polarized emission from liquid crystal polymers," Synth. Met. **111**, 181–185 (2000).
58. M. Sukharev and T. Seideman, "Phase and polarization control as a route to plasmonic nanodevices," Nano Lett. **6**, 715–719 (2006).
59. H. H. Fang, Q. D. Chen, J. Yang, H. Xia, Y. G. Ma, H. Y. Wang, and H. B. Sun, "Two-photon excited highly polarized and directional upconversion emission from slab organic crystals," Opt. Lett. **35**, 441–443 (2010).
60. F. Di Stasio, P. Korniychuk, S. Brovelli, P. Uznanski, S. O. McDonnell, G. Winroth, H. L. Anderson, A. Tracz, and F. Cacialli, "Highly polarized emission from oriented films incorporating water-soluble conjugated polymers in a polyvinyl alcohol matrix," Adv. Mater. **23**, 1855–1859 (2011).
61. C. F. Lai, J. Y. Chi, H. H. Yen, H. C. Kuo, C. H. Chao, H. T. Hsueh, J. F. T. Wang, C. Y. Huang, and W. Y. Yeh, "Polarized light emission from photonic crystal light-emitting diodes," Appl. Phys. Lett. **92**, 243118 (2008).
62. S. R. K. Rodriguez, G. Lozano, M. A. Verschuuren, R. Gomes, K. Lambert, B. De Geyter, A. Hassinen, D. Van Thourhout, Z. Hens, and J. G. Rivas, "Quantum rod emission coupled to plasmonic lattice resonances: a collective directional source of polarized light," Appl. Phys. Lett. **100**, 111103 (2012).
63. H. J. Chen, T. A. Ming, L. Zhao, F. Wang, L. D. Sun, J. F. Wang, and C. H. Yan, "Plasmon-molecule interactions," Nano Today **5**, 494–505 (2010).
64. T. Ming, L. Zhao, H. J. Chen, K. C. Woo, J. F. Wang, and H. Q. Lin, "Experimental evidence of plasmophores: plasmon-directed polarized emission from gold nanorod-fluorophore hybrid nanostructures," Nano Lett. **11**, 2296–2303 (2011).